RSC Advances

PAPER

View Article Online
View Journal | View Issue

Cite this: *RSC Adv.*, 2016, **6**, 2323

Synthesis of a $SrFeO_{3-x}$/g-C_3N_4 heterojunction with improved visible-light photocatalytic activities in chloramphenicol and crystal violet degradation†

Ho-Pan Lin,[a] Chiing-Chang Chen,*[a] Wenlian William Lee,*[b] Ya-Yun Lai,[c] Jau-Yuan Chen,[a] Ya-Qian Chen[a] and Jing-Ya Fu[a]

Received 14th October 2015
Accepted 22nd December 2015

DOI: 10.1039/c5ra21339h

www.rsc.org/advances

Some solid magnetic photocatalysts containing ferrites are convenient for being separated from reaction solutions by a magnet. This study reports the use of the $SrFeO_{3-x}$/g-C_3N_4 photocatalyst heterojunction for the photocatalytic degradation chloramphenicol (CAP) and crystal violet (CV) under visible irradiation. Herein, the novel heterojunction of $SrFeO_{3-x}$/g-C_3N_4 is fabricated by sintering $SrFeO_{3-x}$ with g-C_3N_4. This is the first report of a systematic synthetic study on the preparation and characterization of $SrFeO_{3-x}$/g-C_3N_4 photocatalyst using a sintering method. The photocatalytic activities are evaluated by degrading CAP and CV in aqueous solution induced by visible light. The intermediates formed in the degradation of CAP are separated and identified by HPLC-ESI-MS technique. The quenching effects of different scavengers and EPR display that the reactive $O_2^{\bullet-}$ and $^{\bullet}OH$ radicals play the major roles and h^+ plays a minor role in the CAP degradation. The possible degradation pathways are proposed and discussed in this research. The study is useful to the synthesis of $SrFeO_{3-x}$/g-C_3N_4 and the degradation of CAP and CV for future applications concerning environmental pollution and control.

1. Introduction

The pharmaceutical industry produces a wide variety of products, among which these pharmaceutical products receive extensive concern because of their wide usage worldwide. The existence of pharmaceuticals in the aquatic environment and their possible effects on living organisms are giving rise to growing concern. Many of these samples have been detected in wastewater as well as surface and/or ground waters. These compounds emanate from industrial discharge, hospitals, and domestic sewage.[1–3]

Recently, a number of antibiotics have been detected worldwide in soil, surface water, wastewaters and even drinking water.[1] The residues of antibiotics in environments may cause potential risks to public health. CAP is widely used in the treatment of serious infections, even if recent research revealed serious side effects of CAP on the haemopoietic system, which sometimes accompanied by leucopenia and thrombocytopenia and aplastic anemia.[4] As a consequence, it has been banned for the use in foodstuffs of animal origin in the European Union[5] and United States.[6] However, it is sometimes used topically for eye infections; nevertheless, the global problem of advancing bacterial resistance to newer drugs has led to a renewed interest in its use.[5] Furthermore, in low-income countries, chloramphenicol is still widely used because it is exceedingly inexpensive and readily available.

CAP as a representative antibiotic is applied to inhibiting Gram-positive and Gram-negative bacteria and its residual parts with metabolites from the excrement of human and animals get into the surface water and ground water after the sewage treatment.[4] As a consequence, researchers have been making efforts to find out the ways of inactivating or eliminating the residual parts of CAP. Badawy *et al.*[7] investigated the removal of CAP by Fenton-biological treatment processes. Radiation induced degradation of CAP was studied by Lin *et al.*[8] and Csay *et al.*[9] Recently, much attention has been paid to separate the source of the refractory or toxic effluent and treat it by advanced oxidation processes (AOPs) using homogeneous or heterogeneous catalysts.[10,11] Degradation of CAP using TiO_2 as catalyst has been studied by several researchers.[10,12] However, the previous works are based on the efficiencies and kinetics by changing the parameters and does not consider the various degradation products formed and mechanisms on photocatalytic degradation of CAP.

Triphenylmethane (TPM) dyes are extensively used in the cosmetic, paper, food and leather industries as coloring agents for plastics, oils, fats, waxes, and varnishes.[13] The thyroid

[a]Department of Science Education and Application, National Taichung University of Education, Taiwan

[b]Department of Occupational Safety and Health, Chung-Shan Medical University, Taiwan. E-mail: wllee01@gmail.com

[c]National Tainan Junior College of Nursing, Department of Applied Cosmetology, Taiwan

† Electronic supplementary information (ESI) available. See DOI: 10.1039/c5ra21339h

peroxidase-catalyzed oxidation of TPM dyes in living organisms is of great concern because the oxidation reactions can produce various *N*-dealkylated aromatic amines with structures similar to those of carcinogenic aromatic amines.[14] Recent reports have indicated that TPM dyes can serve as targetable sensitizers in the photodecomposition of specific cells or cellular components.[14] In recent years, photocatalytic processes have been successfully used to degrade TPM dye pollutants.[15,16] In most cases, the reaction kinetics, efficiency, and mechanisms have been well documented.

Recently, an effective and simple strategy to improve the photocatalytic activity of a photocatalyst is the incorporation of a heterostructure, because heterojunctions have great potential for tuning the desired electronic properties of photocatalysts and efficiently separating the photogenerated electron–hole pairs.[17–20]

In the search for robust and stable visible-light-driven semiconductor photocatalysts, a polymeric semiconductor, graphitic carbon nitride (g-C_3N_4), has recently attracted tremendous attention.[21,22] The heptazine ring structure and high condensation degree enable metal-free g-C_3N_4 to possess many advantages such as good physicochemical stability, as well as an appealing electronic structure combined with a medium-band gap (2.7 eV).[23] These unique properties make g-C_3N_4 a promising candidate for visible light photocatalytic applications utilizing solar energy.

It is believed that there is a close relationship between the size, morphology and the properties of photocatalysts. Therefore, photocatalysts with hierarchical architectures are expected to exhibit enhanced photocatalytic performance.[24–27] Recently, TiO_2/g-C_3N_4,[28] $ZnWO_4$/g-C_3N_4,[29] BiOCl/g-C_3N_4,[30] Zn_2GeO_4/g-C_3N_4,[31] BiOBr/g-C_3N_4,[32] CdS/g-C_3N_4,[33] $AgVO_3$/g-C_3N_4,[34] BiOI/g-C_3N_4,[35] $BiOBr_{0.2}I_{0.8}$/g-C_3N_4 (ref. 36) and magnetic MFe_2O_4/graphene[37] composites have been synthesized in order to improve the photocatalytic activity of the materials.

Some solid magnetic photocatalysts containing ferrites are handy to be separated from reaction solution by a magnet.[38] However, no work compared to g-C_3N_4 based on a $SrFeO_{3-x}$ has been reported. It is expected that functionalizing graphitic carbon nitride nanosheets with $SrFeO_{3-x}$ can not only combine both the advantages of $SrFeO_{3-x}$ and graphitic carbon nitride nanosheets but may also result in new properties. The preparation and characterization of $SrFeO_{3-x}$/g-C_3N_4 photocatalyst is the first report demonstrating the systematic synthetic study of $SrFeO_{3-x}$/g-C_3N_4 using sintering method. The photocatalytic activities of $SrFeO_{3-x}$/g-C_3N_4 are evaluated by measuring the degradation efficiencies of CAP, exhibiting excellent activity under visible-light irradiation. Besides, the intermediates in the photocatalytic process are separated, identified, and characterized using HPLC-PDA-ESI-MS to propose the CAP-decomposition mechanism.

2. Experiment

2.1 Materials

Chloramphenicol and sodium azide (Sigma), phenol (Shimakyu), *p*-benzoquinone (Alfa aesar), ammonium oxalate (Osaka), and isopropanol (Merck) were purchased and used without further purification. Reagent-grade sodium hydroxide, nitric acid, ammonium acetate, and HPLC-grade methanol were obtained from Merck.

2.2 Instruments and analytical methods

The field-emission transmission electron microscopy (FE-TEM) images, selected area electron diffraction (SAED) patterns, high resolution transmission electron microscopy (HRTEM) images, and energy-dispersive X-ray spectra (EDS) were obtained using a JEOL-2010 with an accelerating voltage of 200 kV. The Al-Kα radiation was generated at 15 kV. The thermo-gravimetric and differential thermal analysis (TG-DTA; Seiko TG/TGA 300) was carried out in a flow of air (10 mL min^{-1}) at a heating rate of 10 °C min^{-1}. The X-ray diffraction (XRD) patterns were recorded on a MAC Science MXP18 equipped with Cu-Kα radiation, operating at 40 kV and 80 mA. Field emission scanning electron microscopy-electron dispersive X-ray spectroscopy (FE-SEM-EDS) measurements were carried out using a JEOL JSM-7401F at an acceleration voltage of 15 kV. High resolution X-ray photoelectron spectroscopy (HRXPS) measurements were carried out using an ULVAC-PHI. The ultra-violet photoelectron spectroscopy (UPS) measurements were performed using a ULVAC-PHI XPS, PHI Quantera SXM. Photoluminescence (PL) measurements were carried out on Hitachi F-7000. UV-vis diffuse reflectance spectra were recorded on a Scinco SA-13.1 spectrophotometer at room temperature. The Brunauer–Emmett–Teller (BET) specific surface areas of the samples (S_{BET}) were measured with an automated system (Micrometrics Gemini) using nitrogen gas as the adsorbate at liquid nitrogen temperature. The magnetization curves and hysteresis loop of the sample were characterized with a model 4HF vibrating sample magnetometer (ADI) with a maximum field of 18 kOe at room temperature. The HPLC-PDA-ESI-MS system consisted of a Waters 1525 binary pump, 2998 photodiode array detector, and 717 plus autosampler, a ZQ2000 micromass detector.

2.3 Synthesis of g-C_3N_4/$SrFeO_{3-x}$

Under atmosphere conditions, the g-C_3N_4 powder was synthesized by directing calcining melamine in a muffle furnace. In a typical synthesis run, 5 g melamine was placed in a semi-closed alumina crucible with a cover. The crucible was heated to 520 °C for 4 h with a heating rate of 10 °C min^{-1}. After cooling to room temperature, g-C_3N_4 was produced in a powder form.[39] $SrFeO_{3-x}$ was fabricated through sintering method with Fe_2O_3 and $SrCO_3$ at 1000 °C, for 24 h. Herein, the novel heterojunctions of $SrFeO_{3-x}$/g-C_3N_4 were synthesized by sintering $SrFeO_{3-x}$ with g-C_3N_4 at 400–600 °C, 1–3 h.

2.4 Photocatalytic and active species experiments

The CAP (or CV) irradiation experiments were carried out on stirred aqueous solution contained in a 100 mL flask; the aqueous suspension of CAP (or CV) (100 mL, 10 ppm) and the amount of catalyst powder were placed in a Pyrex flask. The pH of the suspension was adjusted by adding either NaOH or HNO_3 solution. Dark experiments were performed in order to examine

the adsorption/desorption equilibrium. 10 mg of the photocatalyst was mixed with 100 mL CAP (or CV) aqueous solution with a known initial concentration, in a 100 mL flask and the mixture shaken in an orbital shaker (100 rpm) at a constant temperature. The mixture was centrifuged at 3000 rpm in a centrifugation machine after batch sorption experiments so that the absorbance of CAP (or CV) could be determined at 296 nm by means of HPLC-PDA-ESI-MS. For visible light experiments a 422 nm cutoff filter was used. Irradiation was carried out using 150 W Xe arc lamps; the light intensity was fixed at 31.2 W m^{-2}, and the reaction vessel was placed 30 cm from the light source. At given irradiation time intervals, a 5 mL aliquot was collected and centrifuged to remove the catalyst. The supernatant was measured by HPLC-PDA-ESI-MS.

A series of quenchers were introduced to scavenge the relevant active species in order to evaluate the effect of the active species during the photocatalytic reaction. $O_2^{\bullet -}$, $^{\bullet}OH$, h^+, and $^1O_2$ were studied by adding 1.0 mM benzoquinone (BQ, a quencher of $O_2^{\bullet -}$),[40] 1.0 mM isopropanol (IPA, a quencher of $^{\bullet}OH$),[41] 1.0 mM ammonium oxalate (AO, a quencher of h^+),[42] and 1.0 mM sodium azide (SA, a quencher of $^1O_2$),[43] respectively. The method was similar to the former photocatalytic activity test.

3. Results and discussion

3.1 Characterization of $SrFeO_{3-x}$/g-C_3N_4 composites

3.1.1 Phase structure. Fig. 1, S1 and S2 of ESI† show the XRD patterns of the as-prepared samples; the patterns clearly show the coexistence of different phases. All the samples as-prepared contain the $SrFeO_{3-x}$ phase (JCPDS 34-0638) and g-C_3N_4 (JCPDS 87-1526), in addition to the $SrCO_3$ (JCPDS 74-1491), and Fe_2O_3 (JCPDS 73-2234) phases. The XRD patterns for 1wt%-500-2, 2wt%-500-2, and 4wt%-500-2 (Fig. 1) are identical to those reported for the $SrFeO_{3-x}$/g-C_3N_4 binary phases; 8wt%-500-2, 10wt%-500-2, and 30wt%-500-2 are identical to those reported for the $SrFeO_{3-x}$/$SrCO_3$/g-C_3N_4 ternary phases; 50wt%-500-2, 70wt%-500-2, and 90wt%-500-2 (Fig. S1 of ESI†) are identical to those reported for the $SrFeO_{3-x}$/$SrCO_3$ binary phases; 4wt%-400-2 and 4wt%-450-2 are identical to those reported for the $SrFeO_{3-x}$/g-C_3N_4; 4wt%-550-2 is identical to those reported for the $SrCO_3$/g-C_3N_4; 4wt%-400-2, 4wt%-450-2, and 4wt%-500-2 are identical to those reported for the $SrFeO_{3-x}$/g-C_3N_4 binary phases; and, 4wt%-600-2 is identical to those reported for the $SrCO_3$/Fe_2O_3 (Fig. S2 of ESI†) binary phases. Table 1 summarizes the results of the XRD measurements.

During the synthetic process, the nucleation and growth of $SrFeO_{3-x}$ grains may preferentially occur on the surface of g-C_3N_4 sheets for the relatively lower nucleation energy of heterogeneous nucleation. The (110) peak of $SrFeO_{3-x}$ in the heterojunctions was much wider than that of pure $SrFeO_{3-x}$, and gradually broadened and shifted with the increase of g-C_3N_4, suggesting a stepwise size decrease of $SrFeO_{3-x}$ in the heterojunctions. This result implies that the crystallite growth of $SrFeO_{3-x}$ along the *c*-axis would be attenuated after being deposited onto g-C_3N_4. In addition, remarkable shift in the (110) peak was observed, suggesting that there was impact on

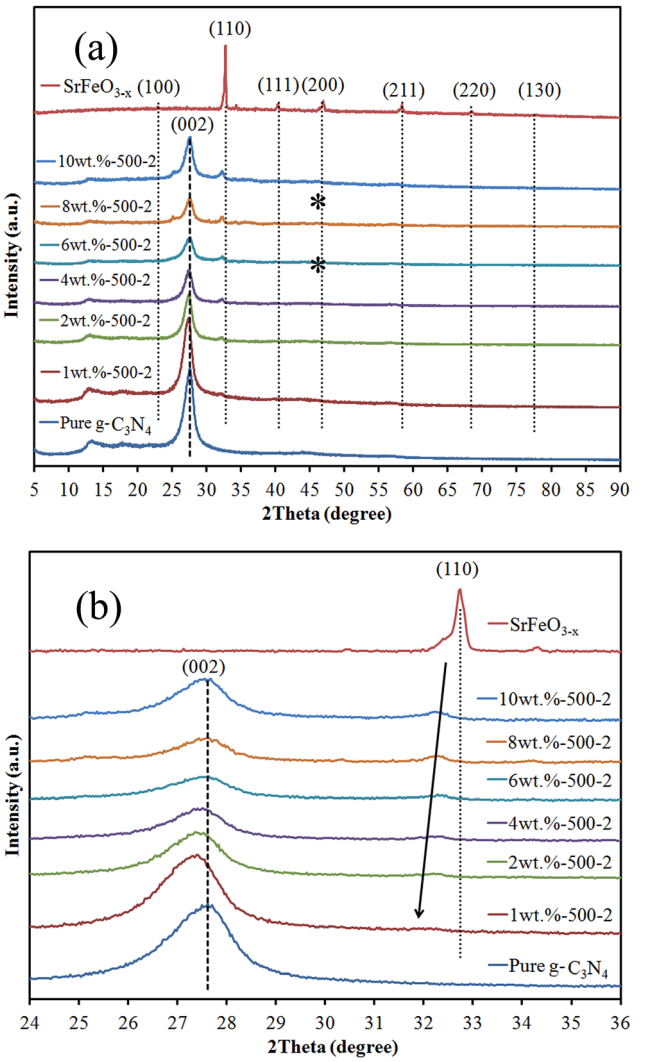

Fig. 1 (a) XRD patterns of as-prepared samples under different weight percentage. (b) Enlarged view (sintering temp = 500 °C, time = 2 h; * impurity phase $SrCO_3$).

the size of the $SrFeO_{3-x}$ in the two-dimensional plane of g-C_3N_4. When $SrFeO_{3-x}$ coupled with g-C_3N_4, it can be found that the (110) peaks of $SrFeO_{3-x}$ and the (002) peak of g-C_3N_4 shifted to 28.1 and 27.3. It implied that the coupling between $SrFeO_{3-x}$ and g-C_3N_4 may be happened on $SrFeO_{3-x}$-(110) facets and g-C_3N_4-(002) facets. After facet coupling between $SrFeO_{3-x}$-(110) and g-C_3N_4-(002), the (110) facets of $SrFeO_{3-x}$ were cover and interaction by g-C_3N_4. So, the intensity of g-C_3N_4-(002) peaks should be decreased and shifted. On the other hand, the half band width of g-C_3N_4-(002) peaks are larger than others, it also accelerate the disappearance of (002) peaks.

Fig. 2 displays that 4wt%-500-2 is composed of differently sized layers, consistent with the TEM observations. In addition, the EDS spectrum shows that the sample contains the elements of Fe, Sr, O, C, and N. The HRTEM image shows that two sets of different lattice images are found with a d-spacing of 0.274 nm, corresponding to the (200) plane of $SrFeO_{3-x}$, which is in good agreement with the XRD results. The results suggest that the

Table 1 Physical and chemical properties of $SrFeO_{3-x}/g\text{-}C_3N_4$ and crystalline phase changes of samples prepared under different reaction conditions

	EDS of atomic ratio (%)					
Photocatalysts	C	N	Sr	Fe	O	XRD pattern
$g\text{-}C_3N_4$	36.49	63.51	—	—	—	$g\text{-}C_3N_4$
$SrFeO_{3-x}$	—	—	16.04	19.39	64.56	$SrFeO_{3-x}$
1wt%-500-2	37.37	58.92	0.06	0.18	3.47	$SrFeO_{3-x}/g\text{-}C_3N_4$
2wt%-500-2	36.79	61.54	0.11	0.23	1.33	$SrFeO_{3-x}/g\text{-}C_3N_4$
4wt%-500-2	34.44	60.52	0.16	0.25	4.63	$SrFeO_{3-x}/g\text{-}C_3N_4$
6wt%-500-2	38.04	60.21	0.37	0.47	1.61	$SrFeO_{3-x}/g\text{-}C_3N_4$
8wt%-500-2	48.84	46.23	0.56	0.62	4.75	$SrFeO_{3-x}/g\text{-}C_3N_4/SrCO_3$
10wt%-500-2	34.97	62.59	1.32	1.82	2.41	$SrFeO_{3-x}/g\text{-}C_3N_4/SrCO_3$
30wt%-500-2	41.43	24.68	7.87	7.24	18.79	$SrFeO_{3-x}/g\text{-}C_3N_4/SrCO_3$
50wt%-500-2	29.06	11.55	10.92	10.13	38.34	$SrFeO_{3-x}/SrCO_3$
70wt%-500-2	20.82	5.90	16.30	17.10	38.87	$SrFeO_{3-x}/SrCO_3$
90wt%-500-2	9.90	2.34	21.67	20.48	45.61	$SrFeO_{3-x}/SrCO_3$
4wt%-400-2	37.31	58.12	0.17	0.27	4.24	$SrFeO_{3-x}/g\text{-}C_3N_4$
4wt%-450-2	35.69	59.88	0.10	0.17	4.16	$SrFeO_{3-x}/g\text{-}C_3N_4$
4wt%-500-2	34.44	60.52	0.16	0.25	4.63	$SrFeO_{3-x}/g\text{-}C_3N_4$
4wt%-550-2	33.15	17.61	4.50	4.78	39.96	$Fe_2O_3/g\text{-}C_3N_4/SrCO_3$
4wt%-600-2	17.22	0.86	15.04	14.74	62.14	$Fe_2O_3/SrCO_3$
4wt%-500-1	41.01	52.20	0.40	0.78	5.61	$SrFeO_{3-x}/g\text{-}C_3N_4$
4wt%-500-1.5	44.25	49.74	0.54	0.44	5.03	$SrFeO_{3-x}/g\text{-}C_3N_4$
4wt%-500-2	34.44	60.52	0.16	0.25	4.63	$SrFeO_{3-x}/g\text{-}C_3N_4$
4wt%-500-2.5	40.12	53.16	0.26	0.40	6.04	$SrFeO_{3-x}/g\text{-}C_3N_4$
4wt%-500-3	40.43	52.58	0.54	0.34	6.11	$SrFeO_{3-x}/g\text{-}C_3N_4$

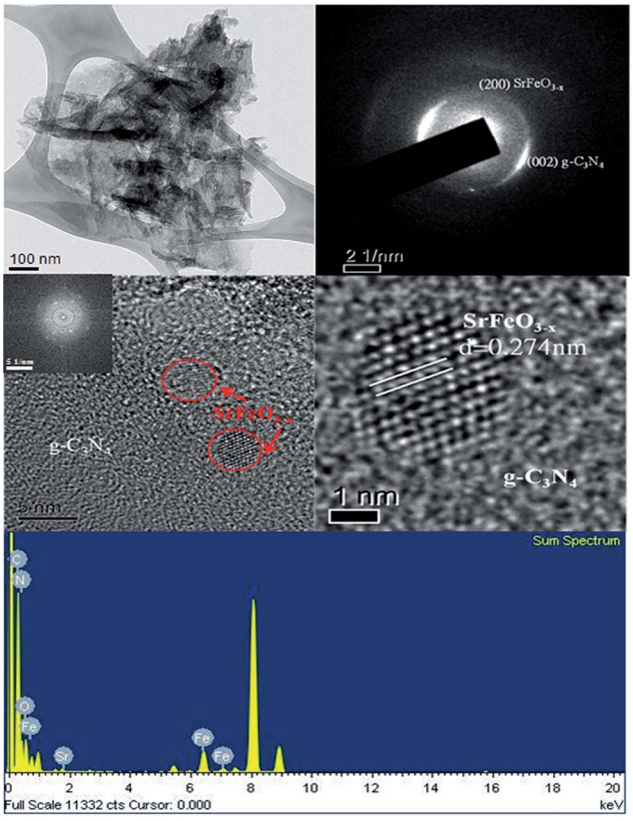

Fig. 2 FE-TEM images and EDS of 4wt%-500-2 sample by the sintering method.

$SrFeO_{3-x}/g\text{-}C_3N_4$ phases have been produced in the composites, which are favorable for the separation of photoinduced carriers, yielding high photocatalytic activities.

Fig. S2 of ESI† reveals the XRD patterns of the 4 wt% $SrFeO_{3-x}/g\text{-}C_3N_4$ samples calcined at different temperatures. The calcination temperature shows a great effect on the powder XRD patterns. When the calcination temperature is higher than 450 °C, the XRD peak of $g\text{-}C_3N_4$ decreases with the increase in calcination temperature and disappears at 600 °C. This result indicates that the heating process at high temperature decreases the $g\text{-}C_3N_4$ content, as confirmed by the TG-DTA experiment (Fig. 3). In Fig. 3(a), the TG-DTA curves of the pure $g\text{-}C_3N_4$ exhibit only one sharp weight loss with one endothermal peak at 725 °C in the temperature range of room temperature to 1000 °C, which may be mainly attributed to the decomposition (or sublimation) of $g\text{-}C_3N_4$ since a large amount of $g\text{-}C_3N_4$ is oxidized. The TG-DTA curves of the physical mixture of $g\text{-}C_3N_4$ and $SrFeO_{3-x}$ (4wt%-500-2) are highly different from those of pure $g\text{-}C_3N_4$.

As shown in Fig. 3(b), two exothermal peaks at approximately 588 °C and 619 °C appear in the DTA curve of the sample, which may be due to the production of $SrCO_3$ and Fe_2O_3. Correspondingly, two weight losses are observed in the TG curve. The total weight loss is 75 wt%, showing that $g\text{-}C_3N_4$ with $SrFeO_{3-x}$ is eliminated for the production of $SrCO_3$ and Fe_2O_3. The result of Fig. 3 clearly reveals that the added $SrFeO_{3-x}$ is a photocatalyst which can absorb and activate the oxygen in the air and then oxidize the $g\text{-}C_3N_4$ at a relatively low temperature.[39] The high temperature can promote oxygen activation. Therefore, the decrease in $g\text{-}C_3N_4$ concentration is more evident in the sample

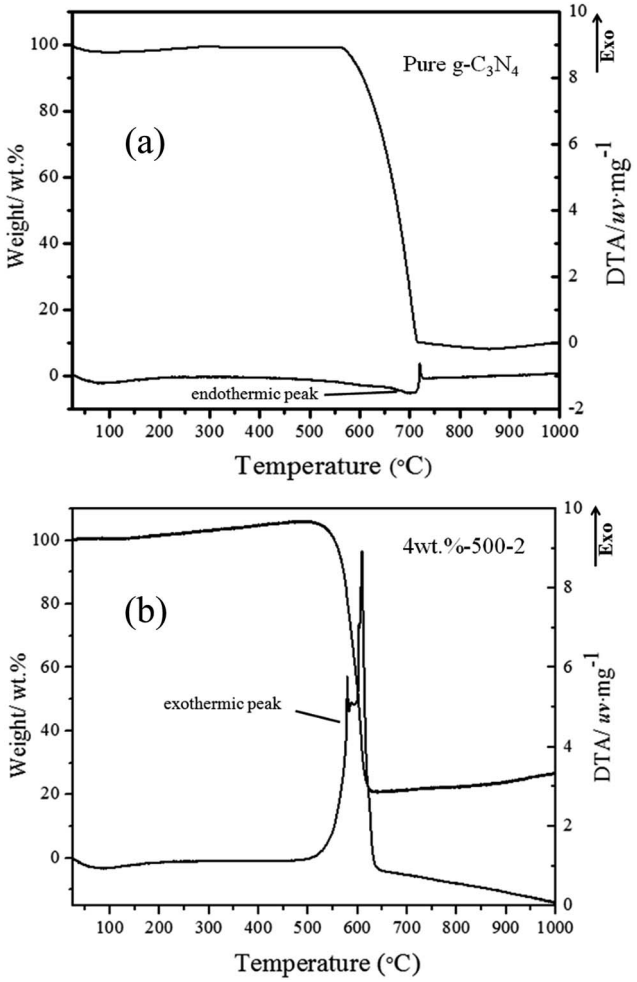

Fig. 3 TG-DTA thermograms for heating (a) the pure g-C_3N_4 and (b) the precursor of 4 wt% $SrFeO_{3-x}$/g-C_3N_4.

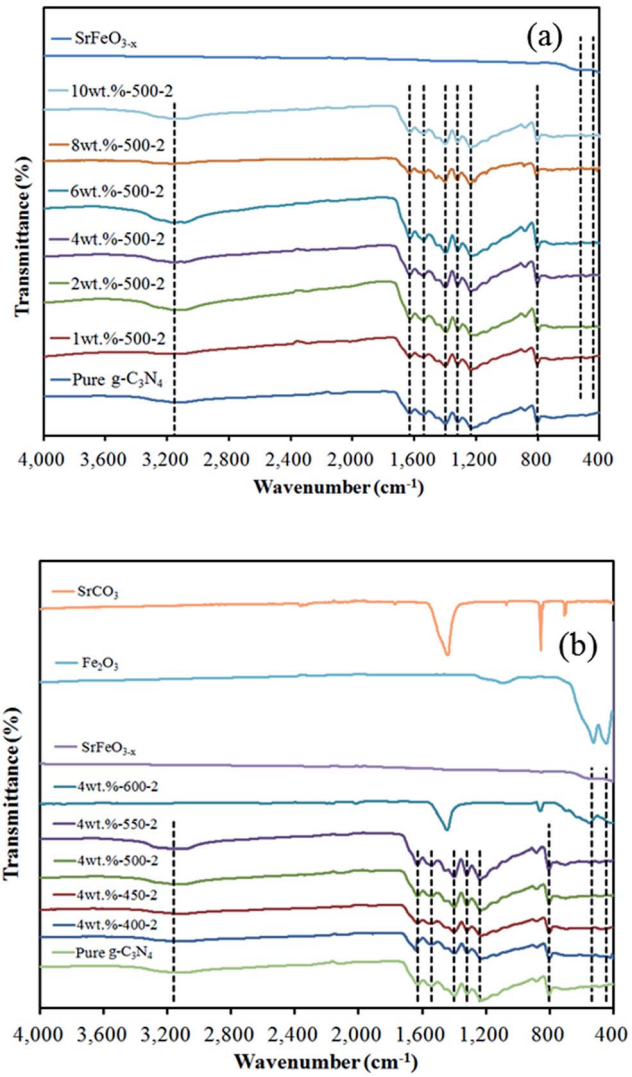

Fig. 4 FT-IR spectra for $SrFeO_{3-x}$/g-C_3N_4 fabricated from different (a) weight percentage and (b) reaction temperature.

sintered at a high temperature. When the mixture is calcined at 638 °C, nearly all of g-C_3N_4 is eliminated and $SrCO_3$ and Fe_2O_3 can be found. The results illustrate that at different reaction temperature, a series of changes happen in the products. The proposed processes for the formation of $SrCO_3$ and Fe_2O_3 are described in eqn (1)–(4).

$$\text{g-}C_3N_4 + SrFeO_{3-x} \rightarrow SrFeO_{3-x}/\text{g-}C_3N_4\ (400\text{–}500\ ^\circ\text{C}) \quad (1)$$

$$\text{g-}C_3N_4 + SrFeO_{3-x} \rightarrow SrCO_3/SrFeO_{3-x}\ (500\text{–}600\ ^\circ\text{C}) \quad (2)$$

$$\text{g-}C_3N_4 + SrCO_3/SrFeO_{3-x} \rightarrow SrCO_3/Fe_2O_3\ (\geqq 600\ ^\circ\text{C}) \quad (3)$$

$$SrCO_3 \rightarrow SrO + CO_2\ (\geqq 1000\ ^\circ\text{C}) \quad (4)$$

Fig. 4 and S3 of ESI† reveal the FT-IR spectra of the $SrFeO_{3-x}$, g-C_3N_4, $SrFeO_{3-x}$/g-C_3N_4, and $SrCO_3$, and Fe_2O_3 composite photocatalysts. The peaks at 442 and 524 cm^{-1} in the $SrFeO_{3-x}$ spectrum correspond to the Fe–O stretching and bending vibrations of the octahedral FeO_6 groups in the perovskite-type structure.[44] The infrared spectrum of a carboxylate group, CO_3^{2-}, displays the characteristically broadened absorption due to the asymmetric and symmetric stretching and bending vibrations at 1443 and 854 cm^{-1} (probably $SrCO_3$).[45] With the relation to pure g-C_3N_4, the peaks at 1251, 1325, 1419, 1571, and 1639 cm^{-1} correspond to the typical stretching modes of the CN heterocycles.[46] Additionally, the characteristic breathing mode of the triazine units at 810 cm^{-1} is observed.[47] The FT-IR spectra of $SrFeO_{3-x}$/g-C_3N_4 symbolize the overlap of the FT-IR spectra of g-C_3N_4 and $SrCO_3$. With the decrease in the g-C_3N_4 concentration or the increase of the calcination temperature, the FT-IR peaks of g-C_3N_4 decrease. This result agrees with that of the XRD experiment.

3.1.2 Morphological structure and composition. $SrFeO_{3-x}$/g-C_3N_4 is synthesized from g-C_3N_4 and $SrFeO_{3-x}$ by sintering methods at different temperature and weight ratios. The surface morphologies of the as-prepared samples (Fig. S4–S8 of ESI†) are measured by FE-SEM-EDS. Table 1 shows that as the weight ratio from 1 to 90 wt%, a gradual change in the atomic ratio of Sr and Fe happens, showing the production of a variety of

compounds in the crystalline phase, including $SrFeO_{3-x}$/g-C_3N_4, $SrFeO_{3-x}$/$SrCO_3$/g-C_3N_4, and $SrFeO_{3-x}$/$SrCO_3$, and as the temperature from 400 to 600 °C, a gradual change in the crystal phases of the reflection peaks happens, showing the production of a variety of compounds in the crystalline phase, including $SrFeO_{3-x}$, g-C_3N_4, and $SrCO_3$, and Fe_2O_3. In Fig. S5 and S6,† the FE-SEM image illustrates that the morphology of the samples prepared with different $SrFeO_{3-x}$/g-C_3N_4 weight percentage changing from irregular nanosheets to irregular microtubes, before changing to micro crystals. In Fig. S7,† the FE-SEM image displays that the morphology of the samples prepared with a same $SrFeO_{3-x}$/g-C_3N_4 weight percentage at different temperature changing from irregular sheets to irregular microtubes, before changing to macro-crystals. In Fig. S8,† the FE-SEM image demonstrates that the morphology of the samples prepared with a same $SrFeO_{3-x}$/g-C_3N_4 weight percentage and temperature at different reaction time changing from irregular micro-crystals to irregular particle, before changing to macro-crystals. The SEM-EDS and TEM-EDS results demonstrate that the main elements within these samples are carbon, nitrogen, strontium, iron, and oxygen at Table 1. From Table 1, the strontium (or iron) atomic ratios (%) of the samples are within the range 0.06–21.67 (or 0.18–20.48), which corresponds to $SrFeO_{3-x}$/g-C_3N_4, $SrFeO_{3-x}$/$SrCO_3$/g-C_3N_4, $SrFeO_{3-x}$/$SrCO_3$, and $SrCO_3$/Fe_2O_3, compared to the stoichiometric ratio (Sr : Fe atomic ratio around 1), and could be selectively synthesized through a sintering method.

3.1.3 X-ray photoelectron spectroscopy analysis. XPS is used for measuring the purity of the prepared samples; the spectra are show in Fig. 5. Fig. 5 presents the C 1s, N 1s, Sr 3d, Fe 2p, and O 1s XPS spectra of the $SrFeO_{3-x}$/g-C_3N_4 samples. Observation of the transition peaks involving the C 1s, N 1s, Sr 3d, Fe 2p, and O 1s orbitals identifies that the catalysts are composed of C, N, Sr, Fe, and O. The structure details about backbone C and N elements in g-C_3N_4 are further researched by their corresponding high resolution spectra. Fig. 5(b) shows the high resolution C 1s spectrum of the $SrFeO_{3-x}$/g-C_3N_4 heterojunction. There are mainly two carbon species displayed in the C 1s spectra: one (284.2 eV) is sp^2 C–C bonds, and the other (287.5 eV) is sp^2-hybridized carbon in N-containing aromatic ring (N–C=N). The latter is indicated as the major carbon species in polymeric g-C_3N_4.[48] In Fig. 5(c), three peaks are deconvoluted for N 1s spectra. The highest peak centering at 398.0 eV is assigned as the sp^2-hybridized nitrogen involved in triazine rings (C–N=C), whereas the peak at 400.3 eV corresponds to the tertiary nitrogen N–$(C)_3$ groups. Both of them, together with sp^2-hybridized carbon (N–C=N, 287.5 eV), compose the heptazine heterocyclic ring units, constructing the basic substructure units of g-C_3N_4 polymers. The weak peak at 403.6 eV is characterized to charging effects or positive charge localization in heterocycles.[49] In Fig. 5(d), the Sr 3d core-level spectra of the samples are satisfactorily assigned to one doublet, attributing that Sr ions are located in same environments. As judged from the BE of the most intense Sr $3d_{5/2}$ peak, it would show that the component at 132.4–132.9 eV comes from Sr ions incorporated into the perovskite structure, whereas that observed at 133.8 eV, which is dominant, can be fitted to $SrFeO_{3-x}$.[50] It is reported that the Fe 2p peaks at binding energies of 711.2 and 725.0 eV with a satellite signal at 719.0 eV are the characteristics of Fe^{3+}, while the peaks at binding energies of 709.9 and 723.4 eV with a satellite signal at 715.5 eV are the characteristics of Fe^{2+}.[51] To the best of our knowledge, the principal features of the Fe 2p-spectra are two maxima reflecting the Fe $2p_{3/2}$ and Fe $2p_{1/2}$ electron levels. Fig. 5(e) shows the XPS spectra of Fe 2p and the deconvoluted peaks. Extraordinary broad peak assigned to $2p_{3/2}$ core levels is observed. The peak of high spin Fe^{3+} ions is broadened significantly compared to Fe^0 and low spin Fe^{2+} state. This broadening is explained by the electrostatic interaction and spin orbit coupling between the 2p core hole and unpaired 3d electrons of the iron ions and crystal field splitting of the 3d orbital into t_{2g} and e_g level.[52] By fitting the peaks for the valence state of Fe ions, the ratio of Fe^{2+}/Fe^{3+} in the $SrFeO_{3-x}$ is calculated as 1 : 3.5, which is similar to the previous report.[53] The asymmetric O 1s peak shown in Fig. 5(f) can be split by using the XPS peak-fitting program. The peak at 532.2 eV is assigned to the external –OH group or the water molecule adsorbed on the surface, and the other O 1s peak appearing at 530.8 eV corresponds to lattice oxygen atoms in the $SrFeO_{3-x}$.[54]

3.1.4 Optical absorption properties. As shown in Fig. S9, S10 and Table S1 of ESI,† the absorption edge of the pure g-C_3N_4 is at about 464.4 nm, which originates from its band gap of ~2.67 eV and is consistent with the reported results.[55] As for the as-prepared $SrFeO_{3-x}$ sample, it clearly exhibits a wide and strong light absorption in the whole UV-vis range of 200–800 nm, which is related to its excellent photocatalytic activity.[56,57] After the introduction of $SrFeO_{3-x}$ particles on the surface of g-C_3N_4, the absorption intensity of these composites is stepwisely strengthened with increasing $SrFeO_{3-x}$ mass ratios. The E_g value of $SrFeO_{3-x}$/g-C_3N_4 is determined from a plot of $(\alpha h\nu)^{1/2}$ *vs.* energy ($h\nu$), which is calculated as 2.54–2.67 eV (Table S1†). The results suggest that the fabrication of the heterostructured $SrFeO_{3-x}$/g-C_3N_4 can greatly improve the optical absorption property and increase the utilized efficiency of solar light, which are favorable for the enhancement of the photocatalytic activity.

3.1.5 Magnetism. Some solid magnetic photocatalysts containing ferrites are convenient to be separated from the reaction solution by a magnet.[38] Magnetic hysteresis measurement for $SrFeO_{3-x}$/g-C_3N_4 heterojunction is carried out in applied magnetic field at room temperature, with the field sweeping from −15 to 15 kOe. The hysteresis loop (Fig. 6) of the sample does not reach saturation up to the maximally applied magnetic field. The magnetization measurement of the sample exhibits a hysteretic feature with the remanent magnetization (M_r) and coercivity (H_c) being determined to be 0.116 emu/g and 1892 Oe, respectively, suggesting that the $SrFeO_{3-x}$/g-C_3N_4 heterojunction exhibits ferromagnetic behaviors at room temperature. This suggests that $SrFeO_{3-x}$/g-C_3N_4 photocatalyst can be easily separated from the solution phase using an external magnet.

3.1.6 Adsorption–desorption isotherm. Fig. S11 and S12 of ESI† show the nitrogen adsorption–desorption isotherm curves of $SrFeO_{3-x}$, g-C_3N_4, and 4 wt% $SrFeO_{3-x}$/g-C_3N_4. The isotherms

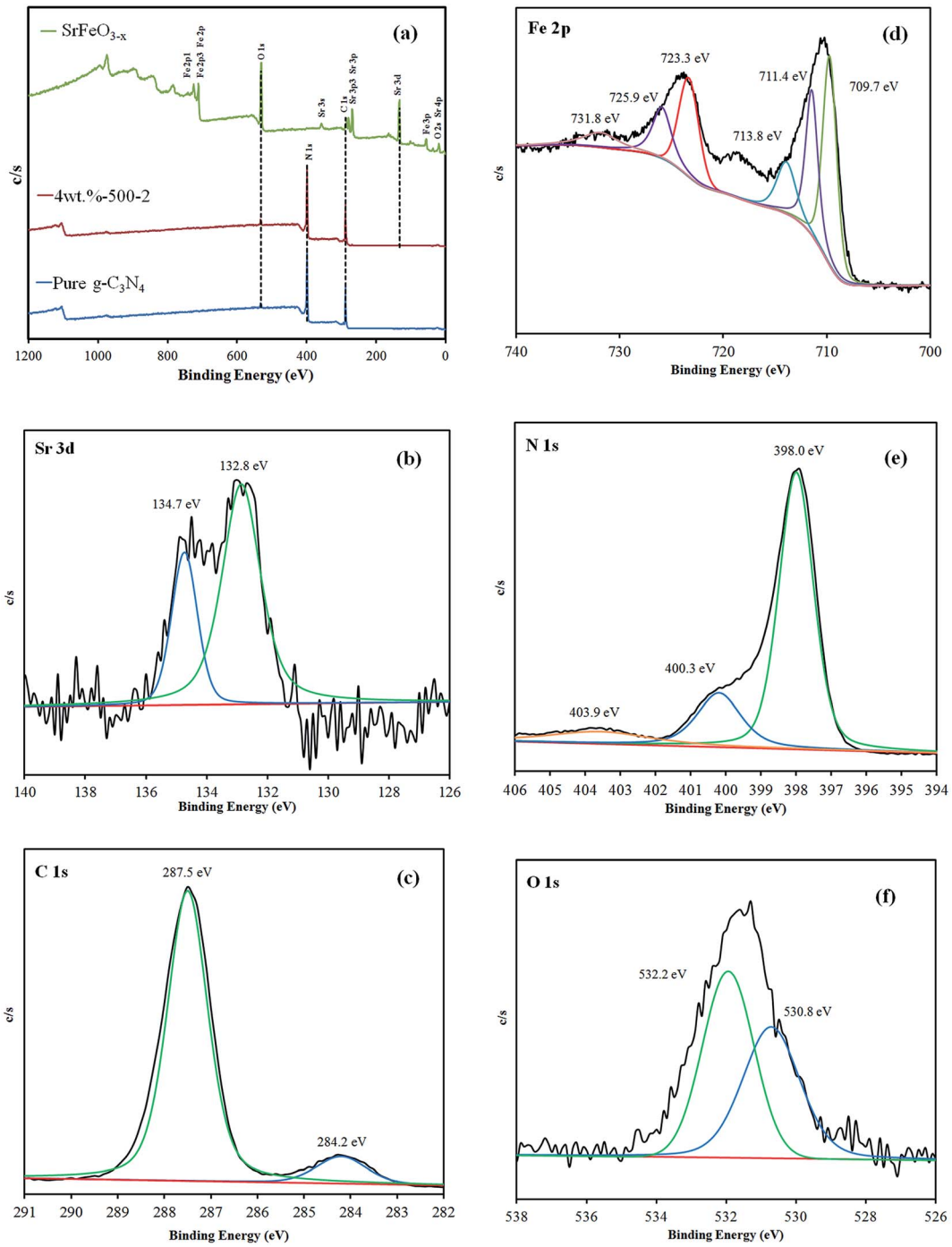

Fig. 5 High resolution XPS spectra of the $SrFeO_{3-x}$, g-C_3N_4, and $SrFeO_{3-x}$/g-C_3N_4 composite: (a) total survey, (b) C 1s, (c) N 1s, (d) Sr 3d, (e) Fe 2p, and (f) O 1s.

of all the samples are close to type IV with a hysteresis loop at a high relative pressure between 0.6 and 1.0.[58] The shape of the hysteresis loop is close to type H3, suggesting the existence of slit-like pores generally formed by the aggregation of plate-like particles, which is consistent with the self-assembled nanoplate-like morphology of samples. This result is consistent with the FE-SEM results, showing that self-assembled nanosheets or nanoplates result in the formation of 3D hierarchical architectures.

3.2 Photocatalytic activity

3.2.1 UV-vis spectra. The changes in the UV-vis spectra during the photodegradation of CAP and CV in aqueous dispersions of 4 wt% $SrFeO_{3-x}$/g-C_3N_4 under visible-light irradiation are illustrated in Fig. 7(a) and (c). After visible-light irradiation for 96 h, *ca.* 91.3% of the CAP is decomposed; and, after irradiation for 12 h, *ca.* 99.9% of the CV is degraded. During visible light irradiation, the characteristic absorption

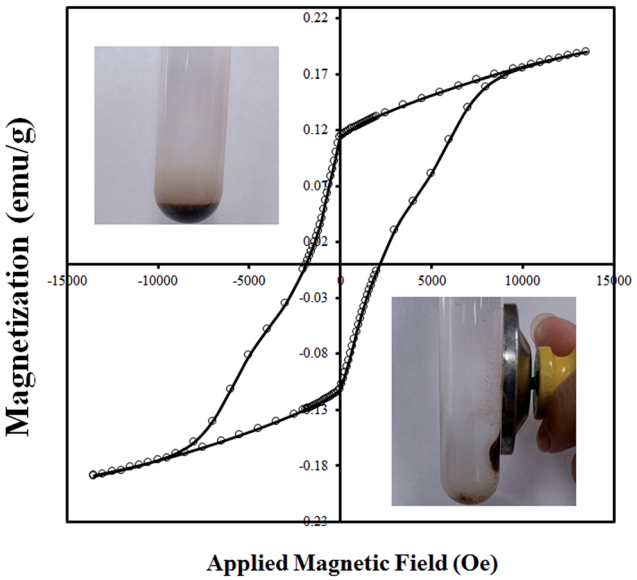

Fig. 6 Hysteresis loop of 4 wt%-500-2 sample measured at 298 K.

band of the CAP around 278 nm decreases rapidly, but no new absorption band appears even in ultraviolet range (340 nm > λ > 200 nm), indicating that there might be the cleavage of phenyl structure of the CAP.[59] During visible light irradiation, the characteristic absorption band of the CV dye around 588 nm decreases rapidly with slight hypsochromic shifts (555 nm), but no new absorption band appears even in ultraviolet range (λ > 200 nm), indicating that there might be the formation of a series of *N*-de-methylated intermediates and cleavage of the whole conjugated chromophore structure of the CV dye. Further irradiation causes the decrease of absorption band at 555 nm, but no further wavelength shift is observed, inferring that the band at 555 nm is that of the full *N*-de-methylated product of the CV dye.

3.2.2 Degradation efficiency. The degradation efficiency as a function of reaction time is illustrated in Fig. 7(b), (d) and S13–S14 of ESI;† the removal efficiency is significantly enhanced in the presence of 4 wt% $SrFeO_{3-x}$/g-C_3N_4. After irradiation for 24 h, 4 wt% $SrFeO_{3-x}$/g-C_3N_4 exhibits a superior photocatalytic performance, with a CAP (or CV) removal efficiency up to 97 (or 95)%. To further understand the reaction kinetics of CV degradation, the apparent pseudo-first-order model expressed by $\ln(C_o/C) = kt$ equation is applied in the experiments.[60] *Via* the first-order linear fit of the data shown in Fig. 7(a), the k value of 4 wt% $SrFeO_{3-x}$/g-C_3N_4 is obtained as the maximum degradation rate of 9.97×10^{-1} h^{-1} using the first-order linear fit of the data, which is much higher than that of the other composites; the 4 wt% $SrFeO_{3-x}$/g-C_3N_4 composite is a much more effective photocatalyst than the others synthesized in this study. Fig. 7(c) shows the photocatalytic efficiency of $SrFeO_{3-x}$/g-C_3N_4 composites and mechanically mixed $SrFeO_{3-x}$ with g-C_3N_4 samples. The photocatalytic efficiency of $SrFeO_{3-x}$/g-C_3N_4 composites significantly increases compared with that of the mechanically mixed sample ($SrFeO_{3-x}$ + g-C_3N_4). Degradation of CAP using TiO_2/g-C_3N_4 composite as catalyst has been studied

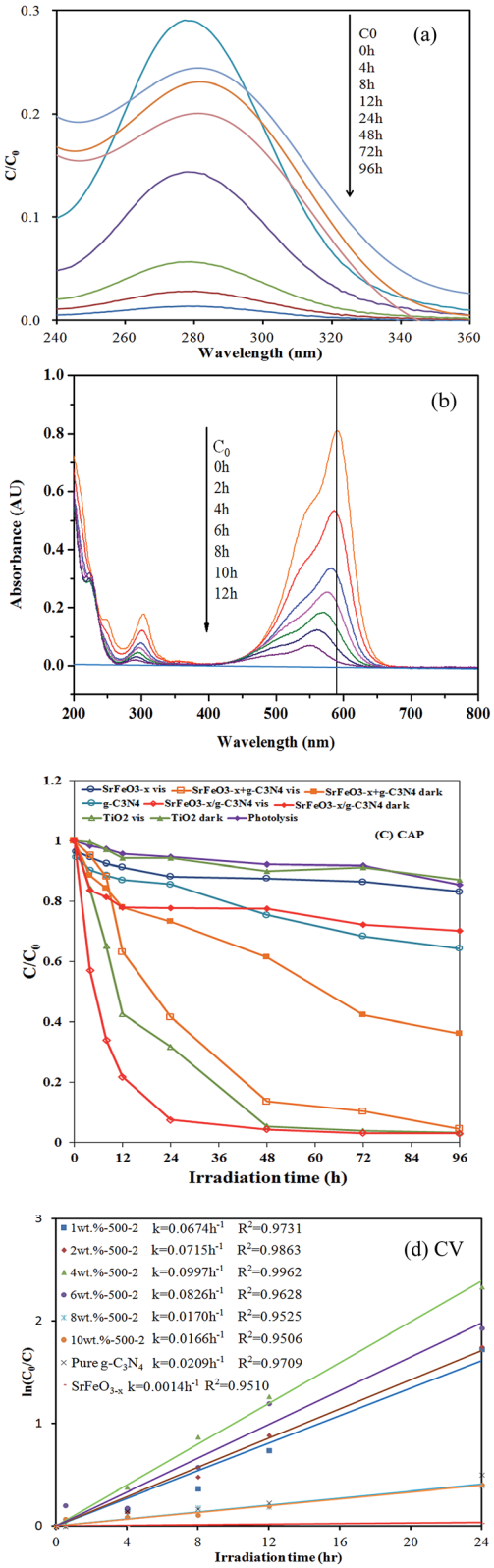

Fig. 7 Temporal UV-vis adsorption spectral changes during the photocatalytic degradation of (a) CAP and (b) CV and photocatalytic degradation of (a) CAP and (b) CV as a function of irradiation time over aqueous $SrFeO_{3-x}$/g-C_3N_4 under visible light irradiation.

by several researchers.[10,12] The disappearance of the organic molecule follows approximately a pseudo-first-order kinetics according to the Langmuir–Hinshelwood model. It was observed that, with P-25 TiO_2 as photocatalyst, quantitative degradation of the organic molecule occurs after 4 h of illumination. However, the previous works are based on the efficiencies and kinetics by changing the parameters and does not consider the various degradation products formed and mechanisms on photocatalytic degradation of CAP. The photocatalytic activity of $SrFeO_{3-x}$/g-C_3N_4 composites reaches the maximum rate constant of 9.97×10^{-1} h^{-1}, 4.8 times higher than that of g-C_3N_4, 2.0 times higher than that of TiO_2.

3.2.3 Brunauer–Emmett–Teller (S_{BET}). The 4 wt% $SrFeO_{3-x}$/g-C_3N_4 composite has larger S_{BET} and pore volume (Table S1 of ESI†). However, the result of Table S1† shows that the 8 wt% $SrFeO_{3-x}$/g-C_3N_4 sample—which shows the highest S_{BET}—does not represent the highest photocatalytic activity among the samples, suggesting that the changes in the photocatalytic activity is resulted from both the S_{BET} and $SrFeO_{3-x}$/g-C_3N_4 composites (or heterojunctions). Therefore, the 4 wt% $SrFeO_{3-x}$/g-C_3N_4 composite shows the best photocatalytic activity. Thus, the $SrFeO_{3-x}$/g-C_3N_4 composites (or heterojunctions) may also play a role in enhancing the photocatalytic activity.

3.2.4 Ion chromatography. The concentrations of Cl^-, NO_3^- and NO_2^- were confirmed using ion chromatography (IC), based on their retention times. An alternative approach for tracking the progress of irradiation time with/without photocatalyst is to monitor the Cl^-, NO_3^- and NO_2^- formed in the solution (Fig. S15 of ESI†). IC analysis showed an increase in the Cl^-, NO_3^- and NO_2^- concentrations at various irradiation times as the photocatalytic and photolysis method progressed. These results indicated initially that Cl^-, NO_3^- and NO_2^- were gradually produced by irradiation as the time gradually increased. The higher the irradiation time was, the higher the Cl^-, NO_3^- and NO_2^- content of the products was. Finally, these ions in the products were fully formatted, resulting in the degradation of CAP under irradiation conditions.

3.2.5 Photoluminescence. As is known, the photocatalysts are excited to generate electron–hole pairs directly after the illumination in the photocatalytic process. Moreover, the photocatalytic efficiency mainly depends on the recombination rate or the lifetime of the photo-generated electron–hole pairs. The faster recombination occurs, the less time is for the chemical reactions. Therefore, PL spectra are utilized for investigating the recombination rate of the photogenerated electron–hole pairs.[47] To investigate the separation capacity of the photogenerated carriers in the heterostructures, the PL spectra of g-C_3N_4, $SrFeO_{3-x}$, and 2–6 wt% $SrFeO_{3-x}$/g-C_3N_4 are measured; the results are shown in Fig. 8. A strong emission peak around 483 nm appears for the as-prepared samples, which could have been derived from the direct electron–hole recombination of band transitions. However, the characteristic emission peak around the lowest intensity 483 nm for the 4 wt% $SrFeO_{3-x}$/g-C_3N_4 indicates that the recombination of photogenerated charge carriers is greatly inhibited. The efficient separation of charge could increase the lifetime of charge carriers and enhance the efficiency of interfacial charge transfer to the adsorbed substrates, thus improving the photocatalytic activity.[61] The lowest relative PL intensities of 4 wt% $SrFeO_{3-x}$/g-C_3N_4 composites, as shown in Fig. 8, suggest that they possess the lowest recombination rate of electron–hole pairs, resulting in their higher photocatalytic activity, as shown in Fig. 7.

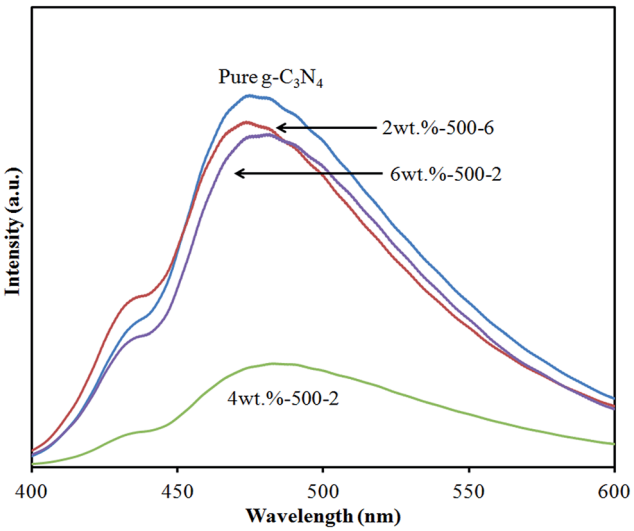

Fig. 8 Photoluminescence spectra of 2wt%-500-2, 4wt%-500-2, 6wt%-500-2, and g-C_3N_4.

3.2.6 Durability of photocatalyst. It can be assumed that the enhanced photocatalytic activities of $SrFeO_{3-x}$/g-C_3N_4 material could be ascribed to a synergistic effect, including high BET surface area, the formation of the heterojunction, layered structure, and the low energy band structure. In the absence of photocatalysts, CV could not be degraded under visible-light irradiation; the superior photocatalytic ability of 4 wt% $SrFeO_{3-x}$/g-C_3N_4 may be ascribed to its efficient utilization of visible light and high separation efficiency of the electron–hole pairs within its composites.

The durability of the 4 wt% $SrFeO_{3-x}$/g-C_3N_4 composite is evaluated by recycling the used catalyst. After each cycle, the catalyst is collected by centrifugation. No apparent loss is observed in the photocatalytic activity when CV is removed in the 3rd cycle; even during the sixth run, the decline in the photocatalytic activity is 5% (Fig. 9(a)). The used 4 wt% $SrFeO_{3-x}$/g-C_3N_4 is also examined by XRD and no detectable difference is observed between the as-prepared and the used samples (Fig. 9(b)); hence, the 4 wt% $SrFeO_{3-x}$/g-C_3N_4 composite has good photostability.

3.3 Photodegradation mechanisms of CAP

In general, three possible reaction mechanisms are proposed to be involved in the photodegradation of organics by a semiconductor, including (i) photocatalysis, (ii) photolysis, and (iii) dye photosensitization.[62] In the photolysis process, a photoinduced electron on the induced organics directly reacts with O_2 to produce a singlet oxygen atom that acts as an oxidant for the pure organic's photolysis.[63] In the experiments, CAP

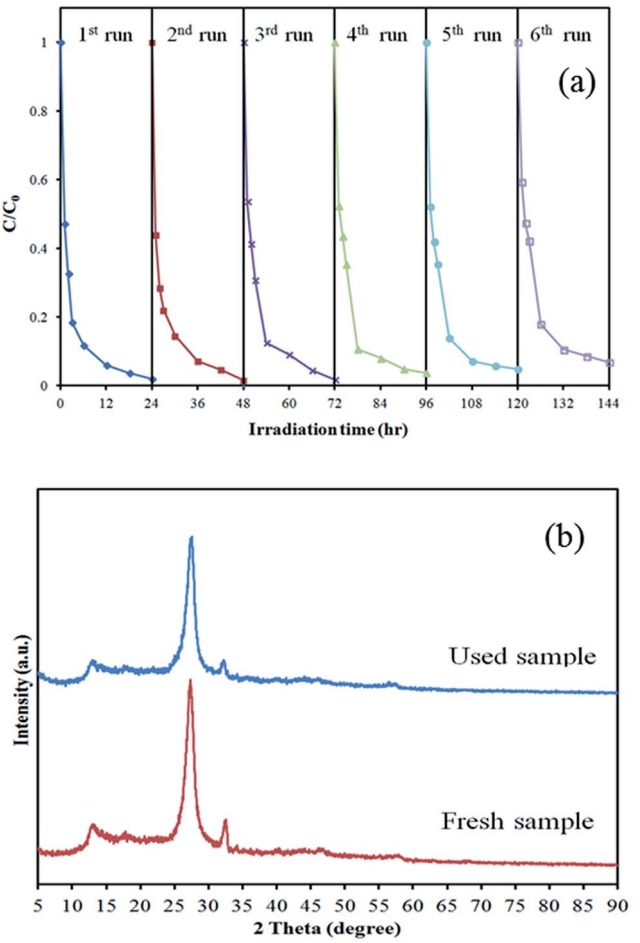

Fig. 9 (a) Cycling runs and (b) XRD patterns acquired before and after the photocatalytic degradation of CAP in the presence of $SrFeO_{3-x}$/g-C_3N_4.

degradation caused by photolysis under visible light in a blank experiment is not observable; CAP is a structure-stable dye and the decomposition by the photolysis mechanism is negligible.

As is known to all, various primary reactive species, such as HO˙, h^+, O_2^{-}˙, H˙ and $^1O_2$, could be generated during photocatalytic degradation processes in the UV-vis/semiconductor systems.[17,18,64–66] In earlier study, CV photodegradation by BiO_mX_n/BiO_pX_q (X, Y = Cl, Br, I) under visible light is dominated by O_2^{-}˙ oxidation being the main active species and ˙OH and h^+ being the minor active species.[16–18] Xiao *et al.* revealed that high-efficiency visible light driven bisphenol-A removal with BiOCl/BiOI could attribute to effective separation and transfer of photoinduced charge carriers in BiOCl/BiOI with narrower band gap and more negative conduction band position, which favored the photogenerated holes.[63] Yu's group reported ˙OH and h^+ being two main actives in the whole degradation process.[67] Shenawi-Khalil *et al.* reported that ˙OH radical was generated by multistep reduction O_2^{-}˙.[68] The generation of O_2^{-}˙ could not only inhibit the recombination of photoinduced charge carriers, but also benefit the de-chlorination of chlorinated phenol derivative. The hydroxyl radical HO˙ might only be formatted *via* an $e^- \rightarrow O_2^{-}$˙ $\rightarrow H_2O_2 \rightarrow$ ˙OH route. Meanwhile, ˙OH radical was formatted by multistep reduction O_2^{-}˙ in the system.[17] Zhu *et al.* reported that photocatalytic experiments in the presence of N_2 and the radical scavenger suggested O_2^{-}˙ and ˙OH being two main actives in the photocatalytic degradation process.[69] Dimitrijevic *et al.*[62] proposed that the water, both dissociated on the surface of TiO_2 and in subsequent molecular layers, had a three-fold role of (i) stabilization of charges, preventing electron–hole recombination, (ii) an electron acceptor, the formation of H atoms in a reaction of photo-generated electrons with protons on the surface, $-OH_2^+$, and (iii) an electron donor, the reaction of water with photo-generated holes to give ˙OH radicals. According to earlier studies,[67] the dominant active oxygen species generated in direct oxidation and photocatalytic reactions were $^1O_2$ and ˙OH radical, respectively. Besides, in this visible light-induced semiconductor system, hydroxylated compounds were also identified for the photocatalytic degradation of CV.[17,18] On the basis of the references presented above, it is proposed that the probability of forming ˙OH should be much lower than that for O_2^{-}˙; however, ˙OH is an extremely strong and nonselective oxidant, which leads to the partial or complete mineralization of several organic chemicals.

3.3.1 Electron paramagnetic resonance. From Fig. 10(a) and (b), not only the four characteristic peaks of DMPO–˙OH adducts (1 : 2 : 2 : 1 quartet pattern) are observed, but also the six characteristic peaks of the DMPO–O_2^{-}˙ adducts are observed under visible light irradiated 4 wt% $SrFeO_{3-x}$/g-C_3N_4 dispersion. Fig. 10(a) and (b) indicates that no EPR signals are observed when the reaction is performed in the dark, while the signals with intensity corresponding to the characteristic peak of DMPO–˙OH and DMPO–O_2^{-}˙ adducts[70] are observed during the reaction process under visible light irradiation, and the intensity gradually increases with the prolonged reaction time, suggesting that $O_2^{\cdot-}$ and ˙OH as major active species are formed in the presence of 4 wt% $SrFeO_{3-x}$/g-C_3N_4 and oxygen under visible light irradiation.

3.3.2 Quenching effect. In order to evaluate the effect of the active species during the photocatalytic reaction, a series of quenchers are introduced to scavenge the relevant active species. As shown in Fig. 10(c), indicating that $^1O_2$ can be negligible, whereas $O_2^{\cdot-}$, ˙OH, and h^+ are important active species in the process of photocatalytic degradation for CAP. Therefore, the quenching effects of different scavengers and EPR display that the reactive $O_2^{\cdot-}$ and ˙OH play the major role and h^+ plays the minor role in the CAP of the photocatalytic degradation.

3.3.3 Scheme for electron–hole separation. The structure characterizations have proven that the $SrFeO_{3-x}$/g-C_3N_4 photocatalyst is a two-phase composite. Considering that the composite presents much higher photocatalytic activity than the component phase alone, it is reasonable that there might have synergetic effect between $SrFeO_{3-x}$ and g-C_3N_4. Actually, many researchers have noted the synergetic effect in composite systems consisting of two semiconductors in contact,[71,72] and attributed the effect to the efficient charge transfer at the interface of two semiconductors, which would result in an effective photoexcited electron–hole separation and,

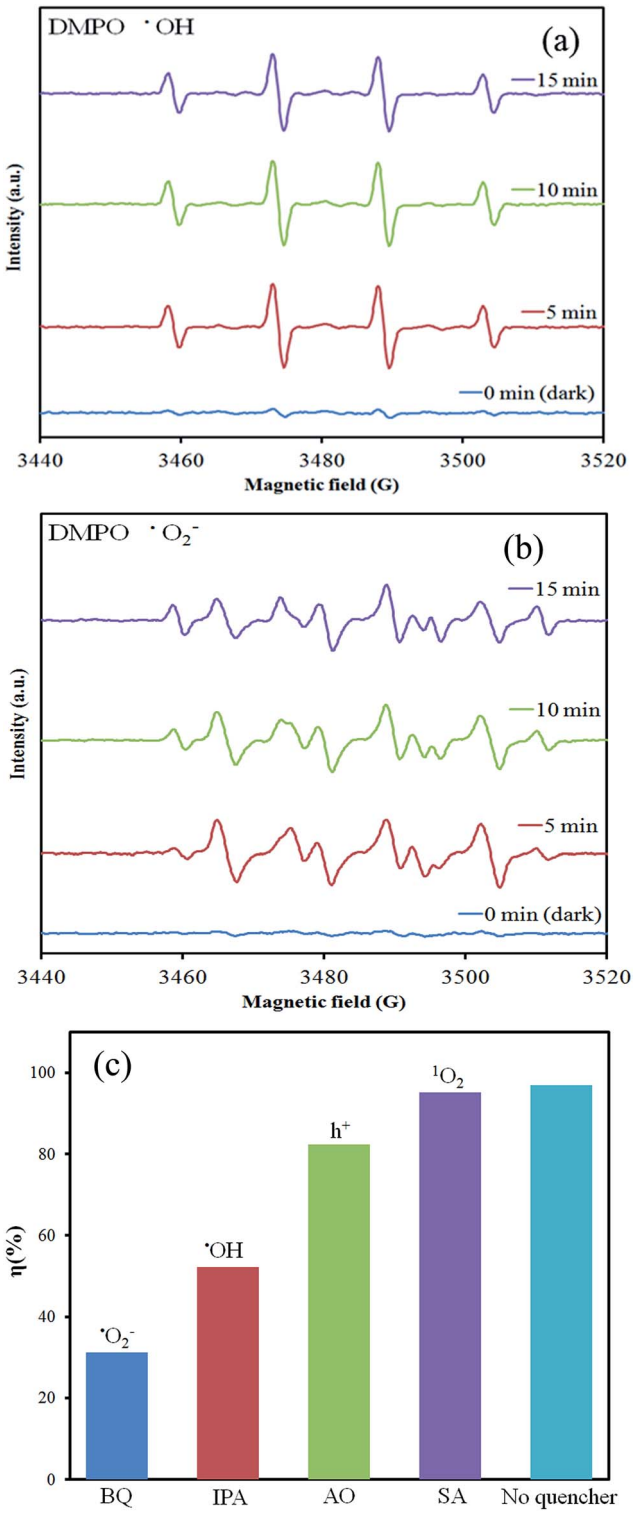

Fig. 10 (a) and (b) DMPO spin trapping EPR spectra for DMPO–$O_2^{\cdot-}$ and DMPO–·OH under visible light irradiation with $SrFeO_{3-x}$/g-C_3N_4 photocatalyst. (c) The dye concentration during photodegradation as a function of irradiation time observed in $SrFeO_{3-x}$/g-C_3N_4 photocatalyst under the addition of different scavengers of SA, IPA, AQ, and BQ.

consequently, enhance the photocatalytic activity. The driving force of charge transfer originates from the matching band potentials. Therefore, the suitable band potential is the precondition for the synergetic effect of composite photocatalysts. Fig. 11 shows the type-II heterostructure band alignment[72] and valence-band (VB) XPS spectrum of $SrFeO_{3-x}$ and g-C_3N_4. In Fig. 11, the position of CB and VB of semiconductor g-C_3N_4 is both higher than that of semiconductor $SrFeO_{3-x}$, and

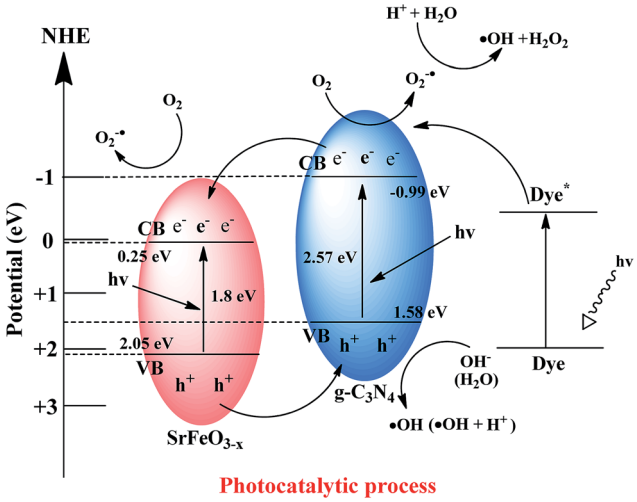

Fig. 11 The band structure diagram of $SrFeO_{3-x}$/g-C_3N_4 and the possible charge separation processes.

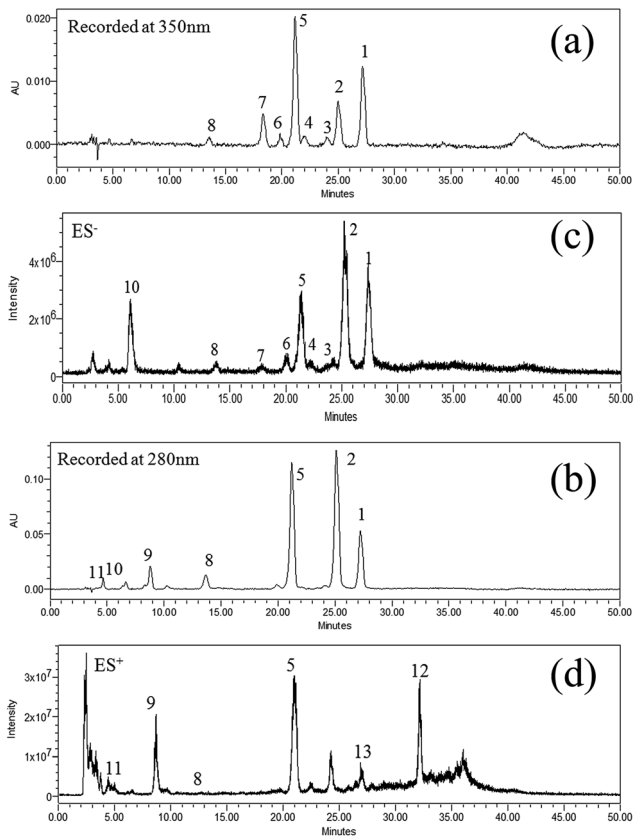

Fig. 12 HPLC chromatogram, recorded at (a) 350 nm, (b) 280 nm, and (c) (d) total ion chromatogram of the degraded intermediates of CAP at different irradiation intervals with $SrFeO_{3-x}$/g-C_3N_4 photocatalyst.

Table 2 The degraded intermediates of CAP by photocatalytic degradation process

Peak no.	MW	λ_{max}, nm	$t_R(ES^-)$	$[M-H]^-$	$t_R(ES^+)$	$[M+H]^+$
1	151	286.5	27.3	150	—	—
2	167	262.8	25.3	166	—	—
3	292	316.3	23.7	291	—	—
4	139	318.7	22.3	138	—	—
5(CAP)	322	274.6	21.4	321	21.5	323
6	338	271.1	20.2	337	20.1	339
7	155	355.8	17.9	154	—	—
8	123	297.2	13.8	122	13.8	124
9	137	286.5	—	—	09.0	138
10	128	267.5	05.6	127	—	—
11	180	287.7	—	—	05.6	181
12	210	—	—	—	27.5	211
13	240	—	—	—	32.6	241

the steps in the CB and VB go in the same direction. The position of the valence band edge of g-C_3N_4 is located at about 1.50 eV, consistent with the result of Falcón *et al.*[73] For $SrFeO_{3-x}$, the VB edge is determined to be 2.05 eV. Therefore, it is obvious that the $SrFeO_{3-x}$ and g-C_3N_4 exhibit suitable band potential. The photoinduced electrons on the g-C_3N_4 particle surface can easily transfer to $SrFeO_{3-x}$ *via* the interfaces, while the holes on the $SrFeO_{3-x}$ surface can migrate to g-C_3N_4 in a similar manner. The charge transfer effectively retards the recombination of electron–hole pairs in the two semiconductors and, thereby improves the photocatalytic efficiency.

3.4 Photodegradation of CAP

3.4.1 Separation and identification of intermediates. So as to get better understanding on the products and the mechanistic details of the photocatalytic degradation of CAP in aqueous g-C_3N_4/$SrFeO_{3-x}$ suspensions under visible light irradiation, the technique of HPLC-PDA-ESI-MS is used for separating the photo-decomposed products and intermediates. According to chromatograms, the CAP and its related intermediates in Fig. 12 can be identified.

As shown in Fig. 12, the ES^- mass spectral analyses confirm the components **1** ($m/z = 150$), **2** ($m/z = 166$), **3** ($m/z = 291$), **4** ($m/z = 138$), **5** ($m/z = 321$), **6** ($m/z = 337$), **7** ($m/z = 154$), **8** ($m/z = 122$), **10** ($m/z = 127$), and the ES^+ mass spectral analyses confirm the components **5** ($m/z = 323$), **6** ($m/z = 339$), **8** ($m/z = 124$), **9** ($m/z = 138$), **11** ($m/z = 181$), **12** ($m/z = 211$), **13** ($m/z = 241$) in Fig. S16 of ESI† and Table 2. Table 2 shows the λ_{max} of UV-visible spectra for peaks 1, 2, 3, 4, 5, 6, 7, 8, 9, 10 being 286.5, 262.8, 316.3, 318.7, 274.6, 271.1, 355.8, 297.2, 286.5, 267.5, 287.7, respectively, and it corresponds to the TIC spectra by retention time. Based on the above experimental results, 12 intermediate products are identified.[60,74] The intermediate product analyses and structures are depicted in Tables 2 and S2 of ESI.†

Fan *et al.* reported[75] that Pt–TiO_2 gathered less negative species on catalyst surfaces, which deteriorated reaction rates, than pure TiO_2 did in an acidic environment. The $^{\bullet}OH$ radical is subsequently produced. The $^{\bullet}OH$ radical is produced subsequently, as also shown in eqn (5)–(10).

$$O_2^{-\bullet} + H^+ + e^- \rightarrow HOO^{\bullet} \quad (5)$$

$$HOO^{\bullet} + H_2O \rightarrow {}^{\bullet}OH + H_2O_2 \quad (6)$$

$$O_2^{-\bullet} + 2H^+ \rightarrow H_2O_2 \quad (7)$$

$$H_2O_2 + e^- \rightarrow {}^{\bullet}OH + OH^- \quad (8)$$

$$h^+ + OH^- \rightarrow {}^{\bullet}OH \quad (9)$$

$$h^+ + H_2O \rightarrow {}^{\bullet}OH + H^+ \quad (10)$$

These cycles continuously happen when the system is exposed to visible-light irradiation;[17,18] after several cycles of photo-oxidation, the degradation of CAP by the generated oxidant species can be expressed by eqn (11)–(13):

$$CAP + h^+ \rightarrow CAP^{+\bullet} \rightarrow \text{degraded compounds} \quad (11)$$

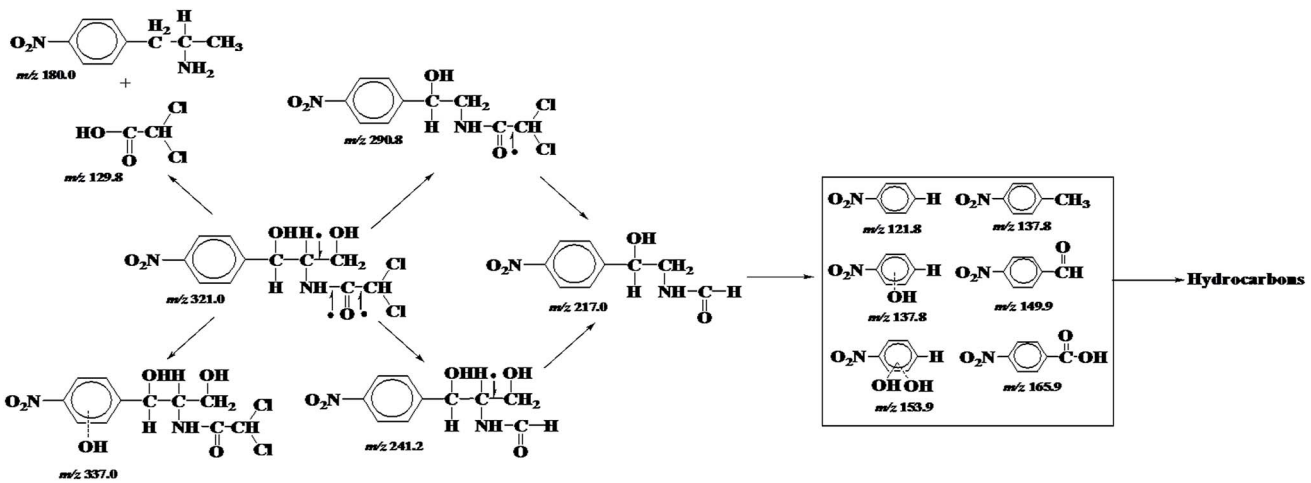

Fig. 13 Proposed photodegradation mechanism of the CAP.

$$CAP + OH^{\bullet}/O_2^{-\bullet} \rightarrow \text{degraded compounds} \quad (12)$$

$$CAP^{+\bullet} + OH^{\bullet}/O_2^{-\bullet} \rightarrow \text{degraded compounds} \quad (13)$$

On the basis of above experimental results, a detailed mechanism of degradation is illustrated in Fig. 13.

4. Conclusions

This is the first report on a series of $SrFeO_{3-x}$/g-C_3N_4 heterojunctions. The removal efficiency is significantly enhanced in the presence of 4 wt% $SrFeO_{3-x}$/g-C_3N_4. The increased photocatalytic activities of $SrFeO_{3-x}$/g-C_3N_4 could be attributed to the formation of the heterojunction between $SrFeO_{3-x}$ and g-C_3N_4, which effectively suppresses the recombination of photoinduced electron–hole pairs. It can be assumed that the enhanced photocatalytic activities of $SrFeO_{3-x}$/g-C_3N_4 materials could be ascribed to the formation of the heterojunction. $O_2^{-\bullet}$ and $^{\bullet}OH$ are main and h^+ is minor active species in the whole process. The reaction mechanisms proposed in this study should offer some useful insight into the future development of technological applications.

Acknowledgements

This research was supported by the Ministry of Science and Technology of the Republic of China (MOST-104-2113-M-142-001).

Notes and references

1 M. Rabiet, A. Togola, F. Brissaud, J. L. Seidel, H. Budzinski and F. Elbaz-Poulichet, *Environ. Sci. Technol.*, 2006, **40**, 5282–5288.
2 A. Y. Lin, T. H. Yu and C. F. Lin, *Chemosphere*, 2008, **74**, 131–141.
3 C. P. Yu and K. H. Chu, *Chemosphere*, 2009, **75**, 1281–1286.
4 Q. Sui, J. Huang, S. B. Deng, G. Yu and Q. Fan, *China Water Res.*, 2010, **44**, 417–426.
5 E. Commission, *Commission Regulation (EC) 1488/94 of 28 June 1994, laying down the principles for the assessment of risks to man and the environment of existing substances in accordance with Council Regulation (EEC) 793/93*, Official Journal of the European Communities L, 1994, p. 161.
6 R. L. Epstein and C. Henry, *J. AOAC Int.*, 1994, **77**, 570.
7 M. I. Badawy, R. A. Waha and A. S. El-Kalliny, *J. Hazard. Mater.*, 2009, **167**, 567–574.
8 L. Lin, S. Yuan, J. Chen, L. Wang, J. Wan and X. Lu, *Chemosphere*, 2010, **78**, 66–71.
9 T. Csay, G. Racz, E. Takacs and L. Wojnarovits, *Radiat. Phys. Chem.*, 2012, **81**, 1489–1494.
10 A. Chatzitakis, C. Berberidou, I. Paspaltsis, G. Kyriakou, T. Sklaviadis and I. Poulios, *Water Res.*, 2008, **42**, 386–394.
11 M. Klavarioti, D. Mantzavinos and D. Kassinos, *Environ. Int.*, 2009, **35**, 402–417.
12 J. Zhang, D. Fu, Y. Xu and C. Liu, *J. Environ. Sci.*, 2010, **22**, 1281–1289.
13 *Ullmann's Encyclopedia of Industrial Chemistry. Part A27. Triarylmethane and Diarylmethane Dyes*, Wiley-VCH, New York, 6th edn, 2001.
14 B. P. Cho, T. Yang, L. R. Blankenship, J. D. Moody, M. Churchwell, F. A. Bebland and S. J. Culp, *Chem. Res. Toxicol.*, 2003, **16**, 285–294.
15 S. T. Huang, Y. R. Jiang, S. Y. Chou, Y. M. Dai and C. C. Chen, *J. Mol. Catal. A: Chem.*, 2014, **391**, 105–120.
16 W. W. Lee, C. S. Lu, C. W. Chuang, Y. J. Chen, J. Y. Fu, C. W. Siao and C. C. Chen, *RSC Adv.*, 2015, **5**, 23450–23463.
17 Y. R. Jiang, H. P. Lin, W. H. Chung, Y. M. Dai, W. Y. Lin and C. C. Chen, *J. Hazard. Mater.*, 2015, **283**, 787–805.
18 T. Li, L. Zhao, Y. He, J. Cai, M. Luo and J. Lin, *Appl. Catal., B*, 2013, **129**, 255–263.
19 Y. Li, L. Fang, R. Jin, Y. Yang, X. Fang, Y. Xing and S. Song, *Nanoscale*, 2015, **7**, 758–764.
20 Y. Yuan, L. Zhang, J. Xing, M. I. B. Utama, X. Lu, K. Du, Y. Li, X. Hu, S. Wang, A. Genç, R. Dunin-Borkowski, J. Arbiol and Q. Xiong, *Nanoscale*, 2015, **7**, 12343–12350.
21 X. Du, G. Zou, Z. Wang and X. Wang, *Nanoscale*, 2015, **7**, 8701–8706.
22 X.-H. Li and M. Antonietti, *Chem. Soc. Rev.*, 2013, **42**, 6593–6604.
23 Z. Zhao, Y. Sun and F. Dong, *Nanoscale*, 2015, **7**, 15–37.
24 W. Wang, M. O. Tadé and Z. Shao, *Chem. Soc. Rev.*, 2015, **44**, 5371–5408.
25 Q. Zhang, Q. An, X. Luan, H. Huang, X. Li, Z. Meng, W. Tong, X. Chen, P. K. Chu and Y. Zhang, *Nanoscale*, 2015, **7**, 14002–14009.
26 X. Lang, X. Chen and J. Zhao, *Chem. Soc. Rev.*, 2014, **43**, 473–486.
27 Y. Fu, T. Huang, L. Zhang, J. Zhu and X. Wang, *Nanoscale*, 2015, **7**, 13723–13733.
28 L. Zhang, D. Jing, X. She, H. Liu, D. Yang, Y. Lu, J. Li, Z. Zheng and L. Guo, *J. Mater. Chem. A*, 2014, **2**, 2071–2078.
29 L. Sun, X. Zhao, C. J. Jia, Y. Zhou, X. Cheng, P. Li, L. Liu and W. Fan, *J. Mater. Chem.*, 2012, **22**, 23428–23438.
30 X. Wang, Q. Wang, F. Li, W. Yang, Y. Zhao, Y. Hao and S. Liu, *Chem. Eng. J.*, 2013, **234**, 361–371.
31 L. Sun, Y. Qi, C. J. Jia, Z. Jin and W. Fan, *Nanoscale*, 2014, **6**, 2649–2659.
32 L. Ye, J. Liu, Z. Jiang, T. Peng, L. Zan, J. Di, J. Xia, S. Yin, H. Xu, L. Xu, Y. Xu, M. He and H. Li, *J. Mater. Chem. A*, 2014, **2**, 5340–5351.
33 J. Yuan, J. Wen, Y. Zhong, X. Li, Y. Fang, S. Zhang and W. Liu, *J. Mater. Chem. A*, 2015, **3**, 18244–18255.
34 T. Zhu, Y. Song, H. Ji, Y. Xu, Y. Song, J. Xia, S. Yin, Y. Li, H. Xu, Q. Zhang and H. Li, *Chem. Eng. J.*, 2015, **271**, 96–105.
35 C. Chang, L. Zhu, S. Wang, X. Chu and L. Yue, *ACS Appl. Mater. Interfaces*, 2014, **6**, 5083–5093.
36 H. Liu, Y. Su, Z. Chen, Z. Jin and Y. Wang, *J. Hazard. Mater.*, 2014, **266**, 75–83.
37 D. Zhang, Q. Wang, L. Wang and L. Zhang, *J. Mater. Chem. A*, 2015, **3**, 3576–3585.
38 Y. Fu, P. Xiong, H. Chen, X. Sun and X. Wang, *Ind. Eng. Chem. Res.*, 2012, **51**, 725–731.

39 B. P. Barbero and L. E. Cadus, *Appl. Catal., A*, 2002, **237**, 263–273.
40 M. C. Yin, Z. S. Li, J. H. Kou and Z. G. Zou, *Environ. Sci. Technol.*, 2009, **43**, 8361–8366.
41 L. S. Zhang, K. H. Wong, H. Y. Yip, C. Hu, J. C. Yu, C. Y. Chan and P. K. Wong, *Environ. Sci. Technol.*, 2010, **44**, 1392–1398.
42 S. G. Meng, D. Z. Li, M. Sun, W. J. Li, J. X. Wang, J. Chen, X. Z. Fu and G. C. Xiao, *Catal. Commun.*, 2011, **12**, 972–975.
43 G. Li, K. H. Wong, X. Zhang, C. Hu, J. C. Yu, R. C. Y. Chan and P. K. Wong, *Chemosphere*, 2009, **76**, 1185–1191.
44 I. A. Leonidov, M. V. Patrakeev, J. A. Bahteeva, E. B. Mitberg, V. L. Kozhevnikov, P. Colomban and K. R. Poeppelmeier, *J. Solid State Chem.*, 2006, **179**, 1093–1099.
45 S. T. Huang, W. W. Lee, J. L. Chang, W. S. Huang, S. Y. Chou and C. C. Chen, *J. Taiwan Inst. Chem. Eng.*, 2014, **45**, 1927–1936.
46 S. C. Yan, Z. S. Li and Z. G. Zou, *Langmuir*, 2009, **25**, 10397–10401.
47 K. Ishibashi, A. Fujishima, T. Watanabe and K. Hashimoto, *Electrochem. Commun.*, 2000, **2**, 207–210.
48 Y. Li, H. Zhang, P. Liu, D. Wang, Y. Li and H. Zhao, *Small*, 2013, **9**, 3336–3344.
49 J. Zhang, M. Zhang, G. Zhang and X. Wang, *ACS Catal.*, 2012, **2**, 2940–2948.
50 H. Falcón, J. A. Barbero, J. A. Alonso, M. J. Martínez-Lope and J. L. G. Fierro, *Chem. Mater.*, 2002, **14**, 2325–2333.
51 N. Wang, L. Zhu, D. Wang, M. Wang, Z. Lin and H. Tang, *Ultrason. Sonochem.*, 2010, **17**, 526–533.
52 A. Jaiswal, R. Das, K. Vivekanand, P. M. Abraham, S. Adyanthaya and P. Poddar, *J. Phys. Chem. C*, 2010, **114**, 2108–2115.
53 F. Yan, M. Lai and L. Lu, *J. Phys. Chem. C*, 2010, **114**, 6994–6998.
54 L. Huang, H. Xu, Y. Li, H. Li, X. Cheng, J. Xia, Y. Xu and G. Cai, *Dalton Trans.*, 2013, **42**, 8606–8616.
55 M. Xu, L. Han and S. Dong, *ACS Appl. Mater. Interfaces*, 2013, **5**, 12533–12540.
56 K. Ji, H. Dai, J. Deng, L. Zhang, F. Wang, H. Jiang and C. T. Au, *Appl. Catal., A*, 2012, **425–426**, 153–160.
57 M. Ghaffari, H. Hunag, O. K. Tan and M. Shannon, *CrystEngComm*, 2012, **14**, 7487–7492.
58 L. Lin, S. Yuan, J. Chen, L. Wang, J. Wan and X. Lu, *Chemosphere*, 2010, **78**, 66–71.
59 T. Csay, G. Racz, E. Takacs and L. Wojnarovits, *Radiat. Phys. Chem.*, 2012, **81**, 1489–1494.
60 A. Chatzitakis, C. Berberidou, I. Paspaltsis, G. Kyriakou, T. Sklaviadis and I. Poulios, *Water Res.*, 2008, **42**, 386–394.
61 S. T. Huang, Y. R. Jiang, S. Y. Chou, Y. M. Dai and C. C. Chen, *J. Mol. Catal. A: Chem.*, 2014, **391**, 105–120.
62 N. M. Dimitrijevic, B. K. Vijayan, O. G. Poluektov, T. Rajh, K. A. Gray, H. He and P. Zapol, *J. Am. Chem. Soc.*, 2011, **133**, 3964–3971.
63 X. Xiao, R. Hao, M. Liang, X. Zuo, J. Nan, L. Li and W. Zhang, *J. Hazard. Mater.*, 2012, **233–234**, 122–130.
64 Y. R. Jiang, S. Y. Chou, J. L. Chang, S. T. Huang, H. P. Lin and C. C. Chen, *RSC Adv.*, 2015, **5**, 30851–30860.
65 J. Wang, Y. Yu and L. Zhang, *Appl. Catal., B*, 2013, **136–137**, 112–121.
66 X. Zhu, J. Zhang and F. Chen, *Appl. Catal., B*, 2011, **102**, 316–322.
67 K. Yu, S. Yang, C. Liu, H. Chen, H. Li, C. Sun and S. A. Boyd, *Environ. Sci. Technol.*, 2012, **46**, 7318–7326.
68 S. Shenawi-Khalil, V. Uvarov, S. Fronton, I. Popov and Y. Sasson, *J. Phys. Chem. C*, 2012, **116**, 11004–11012.
69 X. Zhu, J. Zhang and F. Chen, *Appl. Catal., B*, 2011, **102**, 316–322.
70 X. Xiao, C. Xing, G. He, X. Zuo, J. Nan and L. Wang, *Appl. Catal., B*, 2014, **148–149**, 154–163.
71 H. Li, Y. Zhou, W. Tu, J. Ye and Z. Zou, *Adv. Funct. Mater.*, 2015, **25**, 998–1013.
72 Z. Li, J. Feng, S. Yan and Z. Zou, *Nano Today*, 2015, **10**, 468–486.
73 H. Falcón, J. A. Barbero, J. A. Alonso, M. J. Martínez-Lope and J. L. G. Fierro, *Chem. Mater.*, 2002, **14**, 2325–2333.
74 T. Csay, G. Racz, E. Takacs and L. Wojnarovits, *Radiat. Phys. Chem.*, 2012, **81**, 1489–1494.
75 H. J. Fan, C. S. Lu, W. L. W. Lee, M. R. Chiou and C. C. Chen, *J. Hazard. Mater.*, 2011, **185**, 227–235.

